Technical Appendix

1 Introduction

The Hubbard model offers one of the most simple ways to get insight into how the interactions between electrons can give rise to insulating, magnetic, and even novel superconducting effects in a solid. It was written down in the early 1960's and initially applied to understanding the behavior of the transition metal monoxides (FeO, NiO, CoO), compounds which are antiferromagnetic insulators, yet had been predicted to be metallic by methods which treat strong interactions less carefully.

Over the intervening years, the Hubbard model has been applied to the understanding of many systems, from 'heavy fermions' in the 1980's, to high temperature superconductors in the 1990's, to spin-liquid systems and, in multi-orbital variants, to iron-pnictide and topological materials. Indeed, it is an amazing feature of the model that, despite its simplicity, it exhibits behavior relevant to many of the most subtle and potentially technologically useful properties of solid state physics.

The Hubbard model has been studied by the full range of analytic techniques developed by condensed matter theorists, from simple mean field approaches to field theoretic methods employing Feynman diagrams, expansions in the degeneracy of the number of 'flavors' (spin, orbital angular momentum), etc. It has also been extensively attacked with numerical methods like exact diagonalization and quantum Monte Carlo (QMC) [1–24].

The objective of this technical appendix is to provide an introduction to the Hubbard model and to the quantities of interest to experiment, leaving, however, many of the specific details of engineered Si to the main body of the report. We focus on reviewing the different *computational* approaches. Discussions of analytic methods can be found in [25–28]. For completeness, we begin with a simple introduction of the model, and a discussion of its solution in the non-interacting limit, since this emphasizes the structure of the energy bands and density of states in different geometries which are important as a foundation to the correlation effects.

2 The Hubbard Hamiltonian

The Hubbard Hamiltonian treats the regular array of nuclear positions in a solid as a *fixed* set of lattice sites; in the first of a number of approximations to real solids, it does not account for lattice vibrations. The atoms are further simplified so as to accomodate only a single orbital, which can hold either a spin up or a spin down electron, or both. Acknowledging the screening of the Coulomb potential, the electrons interact with a repulsion U if they sit on the same site. A number of methods are capable of taking longer-range Coulomb interactions also into account, however such calculations are often computationally challenging. The

Correlation	Notation	Operators	Experiment
Greens Function	$A(\mathbf{p},\omega)$	$c_{\mathbf{p},\sigma}$	Angle-Resolved Photoemission
Magnetic Structure Factor	$\tilde{S}(\mathbf{p},\omega)$	$S^+ = c^\dagger_{\mathbf{p},\uparrow} c_{-\mathbf{p},\downarrow}$	Inelastic Neutron Scattering
Conductivity	$\Lambda(\mathbf{p},\omega)$	$j_x = iJ(c^\dagger_{\mathbf{i}+\hat{x}} c_{\mathbf{i}} - c^\dagger_{\mathbf{i}} c_{\mathbf{i}+\hat{x}})$	Optics and Transport
Four Spin correlations	$R(\omega)$	$S^+_{\mathbf{p}} \cdot S^-_{-\mathbf{p}}$	Raman Spectroscopy

Table 1: List of the correlation functions of interest in the Hubbard model (Eqs. 2-6) and their connection to experiment.

kinetic energy consists of an expression which allows electrons to move from one site to its neighbors. The energy scale J which governs this 'hopping' is determined by the overlap of two wavefunctions on the pair of atoms. Since wavefunctions die off exponentially, hopping often is allowed only between the near neighbor sites.

Defining $c^\dagger_{\mathbf{j}\sigma}(c_{\mathbf{j}\sigma})$ to be the operators which create (destroy) electrons of spin σ on lattice site $\mathbf{j}$, the Hubbard Hamiltonian is written as

$$H = -J \sum_{\langle \mathbf{j},\mathbf{l}\rangle \sigma} c^\dagger_{\mathbf{j}\sigma} c_{\mathbf{l}\sigma} + U \sum_{\mathbf{j}} n_{\mathbf{j}\uparrow} n_{\mathbf{j}\downarrow} - \mu \sum_{\mathbf{j}} (n_{\mathbf{j}\uparrow} + n_{\mathbf{j}\downarrow}), \tag{1}$$

where $\langle \mathbf{j},\mathbf{l}\rangle$ denotes that sites $\mathbf{j}$ and $\mathbf{l}$ are nearest neighbors. The situation where the filling is one electron per site is referred to as 'half-filling' since the lattice contains half as many electrons as the maximum number (two per site). On a bipartite lattice, half-filling occurs at chemical potential $\mu = U/2$. Studies of the Hubbard model often focus on the half-filled case because it exhibits Mott insulating behavior and antiferromagnetic order.

The physics of the Hubbard model is encoded in various two particle correlation functions, in particular the space and imaginary time dependent spin-spin correlations,

$$C_{\mathbf{ij}}(\tau) = \langle S^-_{\mathbf{i}+\mathbf{j}}(\tau) S^+_{\mathbf{i}}(0)\rangle \qquad S^+_{\mathbf{i}}(\tau) = e^{\tau \hat{H}}\, c^\dagger_{\mathbf{i}\uparrow} c_{\mathbf{i}\downarrow}\, e^{-\tau \hat{H}}\ , \tag{2}$$

and analogous observables for the charge and pairing,

$$D_{\mathbf{ij}}(\tau) = \langle \rho_{\mathbf{i}+\mathbf{j}}(\tau)\rho_{\mathbf{i}}(0)\rangle - \langle \rho_{\mathbf{i}+\mathbf{j}}(0)\rangle\langle \rho_{\mathbf{i}}(0)\rangle \qquad \rho_{\mathbf{i}}(\tau) = e^{\tau \hat{H}}(c^\dagger_{\mathbf{i}\uparrow} c_{\mathbf{i}\uparrow} + c^\dagger_{\mathbf{i}\downarrow} c_{\mathbf{i}\downarrow}) e^{-\tau \hat{H}} \tag{3}$$

$$P_{\mathbf{ij}}(\tau) = \langle \Delta_{\mathbf{i}+\mathbf{j}}(\tau)\Delta^\dagger_{\mathbf{i}}(0)\rangle \qquad \Delta^\dagger_{\mathbf{i}}(\tau) = e^{\tau \hat{H}}\, c^\dagger_{\mathbf{i}\uparrow} c^\dagger_{\mathbf{i}\downarrow}\, e^{-\tau \hat{H}}\ . \tag{4}$$

On a translationally invariant lattice these correlation functions depend only on the difference $\mathbf{j}$. In the presence of randomness, averaging over different disorder realizations restores translation invariance. These real space quantities can be summed to obtain the structure factors at momenta $\mathbf{p}$. One often focuses on the uniform $[\mathbf{p} = (0,0)]$ and antiferromagnetic $[\mathbf{p} = (\pi,\pi)]$ values.

The correlation functions in imaginary time τ can be integrated to yield magnetic, charge, pairing, and transport susceptibilities. Dynamical properties like the spectral function

$A(\mathbf{p},\omega)$ can be obtained through analytic continuation with the maximum entropy method [18] in cases where the methodology provides data as a function of imaginary time, or more directly with techniques like exact diagonalization. In the former case, for $A(\mathbf{p},\omega)$, we compute the imaginary time dependent Green's function and then invert:

$$G(\mathbf{p},\tau) = \langle\, c_{\mathbf{p}}(\tau)\, c^{\dagger}_{\mathbf{p}}(0)\,\rangle \qquad\qquad G(\mathbf{p},\tau) = \int d\omega\, \frac{e^{-\omega\tau}}{e^{\beta\omega}+1}\, A(\mathbf{p},\omega)\ . \tag{5}$$

For the dynamical spin susceptibility,

$$S(\mathbf{p},\tau) = -\int_{-\infty}^{+\infty} d\omega\ \frac{\mathrm{Im}\,\tilde{S}(\mathbf{p},\omega)\, e^{-\tau\omega}}{1-e^{-\beta\omega}} \tag{6}$$

with analogous expressions for charge $\mathrm{Im}\,\Pi(\omega)$, pairing $\mathrm{Im}\,\mathcal{P}(\mathbf{p},\omega)$, and current $\Lambda(\mathbf{p},\omega)$. The relative sizes of the charge, spin, pairing, and current gaps can be used to distinguish between different types of insulating phases [29].

The more direct procedure for dynamics is described later when details of the exact diagonalization approach are provided.

These quantities directly connect to experimental probes of materials, emphasizing the need to measure dynamics. See Table 1.

3 Limit of No Interactions

In the case of translationally invariant lattices, the Hubbard Hamiltonian is solved analytically by defining creation and destruction operators in momentum space.

$$c^{\dagger}_{\mathbf{p}\sigma} = \frac{1}{\sqrt{N}} \sum_{\mathbf{j}} e^{i\mathbf{p}\cdot\mathbf{j}} c^{\dagger}_{\mathbf{j}\sigma}. \tag{7}$$

Depending on the lattice geometry, there are different dispersion relations which reflect the energy $\epsilon(\mathbf{p})$ associated with momentum $\mathbf{p}$. For example, in the commonly studied case of a square lattice

$$\epsilon(\mathbf{p}) = -2\,J\,\big(\cos p_x + \cos p_y\,\big)$$

The dispersion relation determines the density of states $N(E)$ which counts the number of ways in which the system can have a given energy E.

$$N(E) = \frac{1}{N}\sum_{\mathbf{p}} \delta\big(\, E - \epsilon(\mathbf{p})\,\big).$$

The 'spectral function,' Eq. 5, is the generalization of the density of states to the situation when interactions are turned on ($U \neq 0$) and is one of the central quantities characterizing the metal-insulator transition.

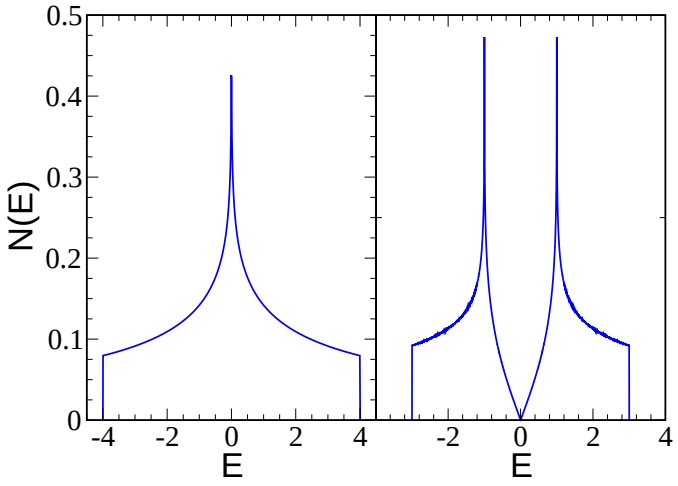

Figure 1: The density of states, $N(E)$ of the square lattice Hubbard model (left) and the honeycomb lattice (right). Note the special features at half-filling ($E = 0$): the van-Hove singularity in the former, and the semi-metallic behavior in the latter.

In many cases, the behavior of the density of states forms the basis of the simplest understanding of the physics of the Hubbard Hamiltonian. On the square lattice, for example, $N(E)$ has a van-Hove singularity (Figure 1, left) at half-filling ($E = 0$) which plays a fundamental role in the critical value of U for which magnetic order onsets. This singularity, along with Fermi surface nesting, was also suggested to have implications for high temperature (cuprate) superconductivity. The density of states of other geometries is also the foundation for determining the properties of associated materials. As an example, the honeycomb lattice of graphene has a linearly vanishing $N(E)$ (see Figure 1, right) associated with the Dirac cones of its dispersion relation. The 'Lieb lattice' which forms the basis of a somewhat more sophisticated description of the CuO_2 sheets of the cuprates hosts a 'flat band' and topologically localized states. In this way, even the simple lattice structure of the Hubbard Hamiltonian can reflect basic band structure of materials, and hence be an appropriate starting point for an understanding of the deeper effects of electron-electron correlations.

With that background, we now turn to methods which can address the effects of those interactions. When possible, we frame our discussion in the language of engineered silicon systems.

4 Exact Diagonalization

For small enough lattices (in particular for small dopant arrays under consideration in this report), the method of choice for solving the Hubbard model is exact diagonalization (ED). In this approach, the Hamiltonian matrix is expressed in some basis (usually the many-body particle number basis for the Fermi-Hubbard model) and is then fully diagonalized. The access to the exact eigenvalues and eigenvectors of the system allows for the calculation of any static or time/frequency dependent quantity, including the transport properties. Certain symmetries of the Hamiltonian and conservation laws, such as the SU(2) symmetry, the

conservation of total number of particles or spin, are used in practice to block diagonalize the matrix and reduce the memory and computational time needed for the diagonalization. The size of the Hilbert space, and hence, the size of the Hamiltonian matrix, grows exponentially with the size of the system and the full diagonalization is simply not feasible beyond ~ 10 sites. For a 10-site system, the matrix corresponding to the sector with 10 particles and a total spin of zero has a dimension of 63504, which would require about 120GB of random access memory (RAM) and a few tens of hours (depending on the processor) to be fully diagonalized using an optimized linear algebra package (LAPACK).

Observables like the charge correlation function of Eq. 2 can easily be expressed in terms of the energy eigenstates $|\psi_\alpha\rangle$ and eigenvalues E_α:

$$\begin{aligned} C_{\mathbf{ij}}(t) = \left\langle\, S^-_{\mathbf{i+j}}(t)\, S^+_{\mathbf{i}}(0)\,\right\rangle &= Z^{-1}\sum_\alpha e^{-\beta E_\alpha}\left\langle\, \psi_\alpha \,\middle|\, S^-_{\mathbf{i+j}}(t)\, S^+_{\mathbf{i}}(0)\,\middle|\, \psi_\alpha\right\rangle \\ &= Z^{-1}\sum_\alpha e^{-\beta E_\alpha}\left\langle \psi_\alpha \,\middle|\, e^{itH}\, S^-_{\mathbf{i+j}}(0)\, e^{-itH}\, S^+_{\mathbf{i}}(0)\,\middle|\psi_\alpha\right\rangle \\ &= Z^{-1}\sum_{\alpha,\beta} e^{-\beta E_\alpha}\left\langle\psi_\alpha\middle| e^{itH} S^-_{\mathbf{i+j}}(0)\,\middle|\psi_\beta\right\rangle\left\langle\psi_\beta\,\middle|\, e^{-itH} S^+_{\mathbf{i}}(0)\,\middle|\,\psi_\alpha\right\rangle \\ &= Z^{-1}\sum_{\alpha,\beta} e^{-\beta E_\alpha}\, e^{it(E_\alpha - E_\beta)}\;\left\langle\psi_\beta\,\middle|\, S^+_{\mathbf{i}}(0)\,\middle|\psi_\alpha\right\rangle\left\langle\psi_\alpha\,\middle|\, S^+_{\mathbf{i+j}}(0)\,\middle|\psi_\beta\right\rangle \end{aligned} \tag{8}$$

where $Z = \sum_\alpha e^{-\beta E_\alpha}$ is the partition function and $\beta = 1/T$ is the inverse temperature.

The appearance of $E_\alpha - E_\beta$ emphasizes connection of the expression for the correlation function to the excitation energy scales in the system. The other key components are the matrix elements of the operators to be measured. The strength of the exact diagonalization approach is the ability to access these quantities directly, without recourse to methods like analytic continuation.

For large diagonalizations such as the one mentioned above for a 10-site system, one may take advantage of multi-threaded features in Intel's math kernel library (MKL) in case of large number of processors per node, or distributed-memory linear algebra packages, such as ScaLAPACK, which can employ massively parallel environments to reduce the computational time, and get around memory issues by distributing the Hamiltonian and other large matrices between nodes during the calculation.

Full diagonalization scales as $O(N^3)$, where N is the matrix dimension. The same scaling applies to the calculation of the dynamical correlation functions after the diagonalization step, often with a much larger prefactor. In those cases, parallel schemes, such as message passing interface (MPI) or OpenMP can be utilized to distribute the computation load.

Results for the Hubbard model on system sizes that can be exactly diagonalized are expected to vary significantly depending on the size and geometry of the clusters considered. Those changes are expected to be especially notable in the weak-coupling region where the strength of the interaction strength is smaller than the noninteracting bandwidth. However, this can be advantageous in comparing with experiments on dopant arrays since currently available systems are far from the thermodynamic limit and each can have a unique geometry and set of model parameters. Another advantage of exact diagonalization over most other numerical methods for the Hubbard model is that any geometry and virtually any variant of the model

can be simulated. This is especially useful for dopant arrays since hopping amplitudes or Coulomb interactions are expected to extend up to a few dopant sites in range.

5 The Lanczos Algorithm

Current experiments with dopant arrays on Si can be done at extremely low temperatures, one of their major potential advantages over optical lattices. In cases where only the ground state, or even a few excited states, are sufficient to estimate properties at experimentally relevant temperatures, one can take advantage of the Lanczos algorithm to go to larger system sizes. The Lanczos algorithm offers an iterative method to diagonalize huge matrices,

$$\begin{aligned} H\left|\Phi_1\right\rangle &= e_1\left|\Phi_1\right\rangle + b_2\left|\Phi_2\right\rangle \\ &\cdots \\ H\left|\Phi_n\right\rangle &= e_n\left|\Phi_n\right\rangle + b_{n+1}\left|\Phi_{n+1}\right\rangle + b_n\left|\Phi_{n-1}\right\rangle \end{aligned} \tag{9}$$

based on the recurrent procedure

$$\begin{aligned} e_n &= \left\langle\Phi_n\right| H\left|\Phi_n\right\rangle \\ \left|\Phi_{n+1}\right\rangle &= H\left|\Phi_n\right\rangle - e_n\left|\Phi_n\right\rangle - b_n\left|\Phi_{n-1}\right\rangle\ . \end{aligned} \tag{10}$$

By keeping only a few arrays of size N during the calculation, one can access a limited, but nevertheless highly useful portion of the spectrum- the ground state and low-lying excited states. Through the successive operation of the Hamiltonian on an initially random state in Eq. 9, the basis is transformed to the basis for a Krylov subspace in which the matrix is tridiagonal, much smaller in dimension, and with a spectrum that approaches that of the original matrix starting at the ground state as the number of iterations increases. A simple QR algorithm can then diagonalize the tridiagonal matrix to obtain the lowest eigenvalues.

There are well-known stability issues associated with the Lanczos algorithm, preventing one from continuing the iterative process to obtain the full spectrum. Often these issues are caused by the loss of orthogonalization between basis vectors of the new subspace, which can be overcome by keeping more vectors of size N during the calculation and adding an increasingly expensive re-orthogonalization step as the number of iterations is increased. Nevertheless, the algorithm remains a powerful one for the low-temperature physics of quantum lattice models.

6 Numerical Linked Cluster Expansions

In numerical linked-cluster expansions (NLCEs) [30–33] an extensive property of the model on a finite or infinite lattice is expressed as a sum over contributions from all the clusters that can be embedded in the lattice.

$$P = \frac{1}{L}\sum_c W_P(c), \tag{11}$$

where P is the extensive property per site, L is the system size (can be infinity), and $W_P(c)$ is the contribution to property P from cluster c. The system is either in the thermodynamic limit or is larger than what can be treated exactly, for example using exact diagonalization. In the case of infinite lattice size, the factor $\frac{1}{L}$ can be removed if we consider the contributions only from those clusters that are not related through translational symmetry. If the model retains the underlying point-group symmetries of the lattice, the contributions from all the clusters that are related by point-group symmetry transformations can also be combined.

The contribution of each cluster $W_P(c)$ is calculated through the inclusion-exclusion principle and using the exact knowledge of the property on that cluster and smaller clusters via ED.

$$p(c) = \sum_{s \subseteq c} W_P(s) \qquad\qquad W_P(c) = p(c) - \sum_{s \subset c} W_P(s), \tag{12}$$

where the sum runs over the cluster c and all of its sub-clusters s. Starting from the smallest cluster in the expansion (typically a single site) for which $\sum_{s \subset c} W_P(s) = 0$, one can obtain $W_P(c)$ for larger clusters up to a certain size until $p(c)$ can no longer be exactly known. Exact diagonalization is used to calculate $p(c)$.

NLCEs can enjoy many of the advantages of the ED, e.g., virtually any model can be simulated and one has access to the full partition function and all the static and time-dependent correlation functions. The series, in its region of convergence, also produces exact results with no systematic or statistical errors. That is especially useful when it is written for the lattice model in the thermodynamic limit. The main disadvantage can be the limitation in temperature. For models with divergent correlations in the ground state, the convergence of the series is lost below the temperature where the correlation length grows beyond the order of the largest clusters in the series. For the uniform Hubbard model in the thermodynamic limit with a repulsive interaction, the dominant correlations at low temperatures are antiferromagnetic with an exchange constant that is inversely proportional to the interaction U in the strong-coupling regime. Therefore, the lowest convergence temperature in the NLCE decreases with increasing U at half filling and can be lower than what quantum Monte Carlo methods can reliably access due to sampling issues that arise at large U [34–36].

NLCEs can be utilized to calculate thermodynamic as well as transport properties (see Sec. 10) of the dopant arrays in Si for sizes larger than those that can be solved using ED. Since there can be significant disorder in the model parameters, leading to an entanglement that will likely remain short ranged even at the lowest temperatures, it would not be unexpected to find that the NLCE with a finite number of terms converges in a wide range of temperatures, perhaps including the ground state.

7 Determinant Quantum Monte Carlo

In the determinant QMC method [1], a path integral for the partition function Z is constructed by discretizing the inverse temperature $\beta = L\Delta\tau$, so that the full imaginary time evolution operator can be written as the product of L terms. The small parameter $\Delta\tau$ allows for the 'Trotter approximation' to separate the exponential of the kinetic $\hat{K}$ (the terms including the hopping J and chemical potential μ) and potential $\hat{V}$ (involving the

on-site Hubbard interaction U) energies:

$$Z = \mathrm{Tr}\left[e^{-\beta\hat{H}}\right] = \mathrm{Tr}\left[e^{-\Delta\tau\hat{H}}\cdots e^{-\Delta\tau\hat{H}}\right] \approx \mathrm{Tr}\left[e^{-\Delta\tau\hat{K}}e^{-\Delta\tau\hat{V}}\cdots e^{-\Delta\tau\hat{K}}e^{-\Delta\tau\hat{V}}\right] \qquad (13)$$

On every site $\mathbf{j}$ and imaginary time slice τ, the terms $e^{-\Delta\tau\hat{V}}$ are rewritten via the discrete Hubbard-Stratonovich transformation [37]

$$e^{-U\Delta\tau\, n_\uparrow n_\downarrow} = \frac{1}{2}\, e^{-U\Delta\tau\,(n_\uparrow+n_\downarrow)/2} \sum_{S=\pm 1} e^{\lambda S\,(n_\uparrow - n_\downarrow)} \qquad (14)$$

so that up and down fermions no longer couple to each other but instead move in a space and imaginary time dependent auxiliary field $S(\mathbf{j},\tau)$. The coupling constant λ obeys $\cosh\lambda = e^{U\Delta\tau/2}$. This transformation converts Eq. 13 into a trace over quadratic forms of the fermion opperators, and allows them to be integrated out analytically, resulting in the product of the determinants of two matrices M_σ, one for each spin species. The partition function $Z = \mathrm{Tr}\, e^{-\beta\hat{H}}$ is then a sum over all configurations of the Hubbard-Stratonovich field, which is sampled stochastically with both single spin flip moves [1] and 'global' updates which decrease autocorrelation time [38].

DQMC allows the exact solution of tight binding Hamiltonians like Eq. 1 on finite spatial clusters, up to statistical errors generated by the Monte Carlo sampling. Systematic 'Trotter errors' from the discretization of β can be extrapolated to zero [39–41]. Continuous time methods also exist, in related algorithms. These methods are advantageous since there is no Trotter error [42–44], especially when quantities of very high precision such as energy and double occupancy are being measured. DQMC currently allows simulations of several hundred up to one thousand spatial sites, depending on the strength of U and the inverse temperature [45], and order of magnitude larger than exact diagonalization. The chief limitation of DQMC is the sign problem [46–52]. Constrained path methods have been developed to address the sign problem in DQMC. However, they rely on an approximation in the form of assuming a particular structure for the nodes of the fermion wave function [20].

The matrix inverses $G_{\mathbf{j}\sigma} = M^{-1}_{\mathbf{j}\sigma}$ are the single particle fermion Green's functions. Their matrix elements directly determine the density and kinetic energy. The double occupancy, and, indeed all the various spin, charge and pairing correlations of Eqs. 2,4 are obtained by averaging appropriate product of elements of $G_\uparrow G_\downarrow$.

8 Dynamical Mean Field Theory and its Cluster Extensions

Conventional 'static' mean field theory (MFT) was one of the earliest methods used to solve the Hubabrd Hamiltonian. The approach begins by decoupling the interaction term, $U n_{\mathbf{j}\uparrow}\, n_{\mathbf{j}\downarrow} \rightarrow U(\, n_{\mathbf{j}\uparrow}\,\langle n_{\mathbf{j}\downarrow}\rangle + \langle n_{\mathbf{j}\uparrow}\rangle\, n_{\mathbf{j}\downarrow} - \langle n_{\mathbf{j}\uparrow}\rangle\,\langle n_{\mathbf{j}\downarrow}\rangle\,)$. After making a specific *ansatz* for the averages $\langle n_{\mathbf{j}\sigma}\rangle$, the resulting Hamiltonian is then quadratic in the fermion operators and can be diagonalized. The physics is determined by finding the expectation values which minimize the free energy, or, equivalently, a self-consistent computation of $\langle n_{\mathbf{j}\sigma}\rangle$. Static MFT can be used to determine magnetic and charge order (and, indeed, provided some of

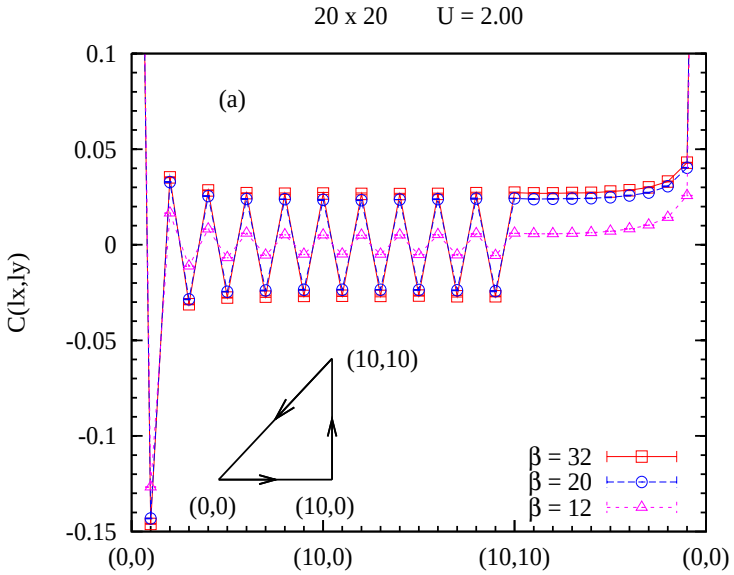

Figure 2: DQMC results for the equal time magnetic correlations $C_{\mathrm{i,j}}(\tau = 0) = \langle S^-_{\mathbf{i+j}}(0)\, S^+_{\mathbf{i}}(0)\rangle$ for $\mathbf{j} = \mathbf{i} + (l_x, l_y)$ (see Eq. 2). Simulations were done on a 20x20 lattice at $U/t = 2$ and three inverse temperatures β. As β increases, long range antiferromagnetic correlations develop.

the first indications of 'stripe' formation [53]), but suffers some very serious limitations. It tends to grossly overestimate the tendency for ordered phases. Even more significantly, since static MFT reduces the problem to noninteracting electrons coupled to average densities, the resulting excitations have infinite lifetime.

This latter problem is rectified by Dynamical Mean Field Theory (DMFT) [54–63]. The basic idea of DMFT is to replace the full lattice problem of Eq. 1 with a single-site 'impurity' problem in which the local Green's function is determined self-consistently. The mean field with which the impurity couples is allowed to fluctuate in imaginary time so that DMFT better models the effects of the electron-electron interaction U.

The Anderson Impurity Model (AIM) onto which DMFT maps the Hubbard Hamiltonian is given by,

$$H = \sum_{\mathbf{p}} \epsilon_{\mathbf{p}}\, a^\dagger_{\mathbf{p}} a_{\mathbf{p}} + \sum_{\mathbf{p}\sigma} V_{\mathbf{p}\sigma}\left(a^\dagger_{\mathbf{p}\sigma} c_\sigma + c^\dagger_\sigma a_{\mathbf{p}\sigma}\right) + U n_\uparrow n_\downarrow - \mu(n_\uparrow + n_\downarrow) \tag{15}$$

which describes a single electron mode (c_σ) hybridized with a bath ($a_{\mathbf{p}\sigma}$). This AIM can be solved via a variety of techniques including the numerical renormalization group, iterated perturbation theory, the non-crossing approximation, and continuous time QMC, the last of which being the most challenging computationally, but at the same time the least biased. These methods yield the impurity Greens function $G_{\mathrm{imp}}(\tau) = \langle\, \mathcal{T} c(\tau) c^\dagger(0)\,\rangle$ (where $\mathcal{T}$ is the imaginary time ordering operator) whose Fourier transform is,

$$G_{\mathrm{imp}}(i\omega_n) = \sum_{\mathbf{p}} \frac{1}{i\omega_n + \mu - \epsilon(\mathbf{p}) - \Sigma(\mathbf{p}, i\omega_n)} \tag{16}$$

The DMFT approximation is the replacement of $\Sigma(\mathbf{p}, i\omega_n)$ by $\Sigma(i\omega_n)$, i.e. ignoring the momentum dependence of the self-energy. The DMFT equations are solved self-consistently from a starting guess for $\Sigma(i\omega_n)$. DMFT can be shown to provide an exact solution of the Hubbard Hamiltonian in the limit of infinite dimension [54, 58].

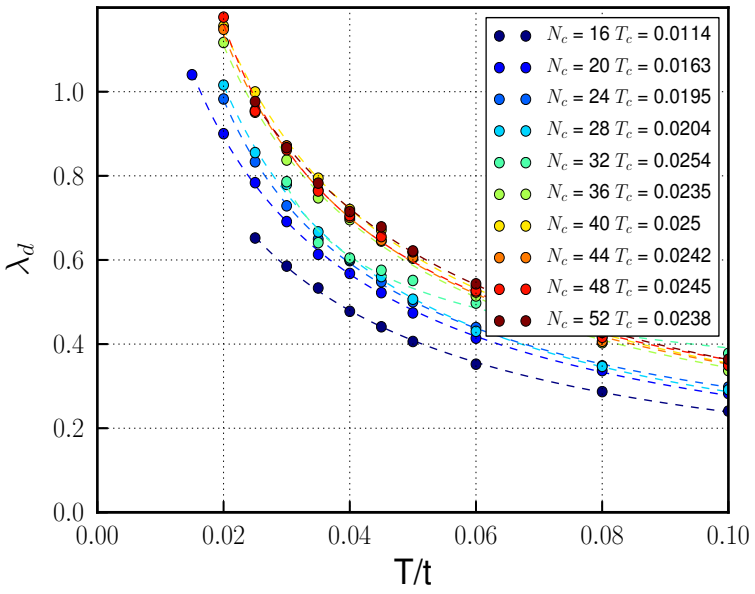

Figure 3: The d-wave eigenvalue of the 2D Hubbard model for U/J=4 and filling $\langle n \rangle$ =0.9. Data for different cluster sizes Nc converge to $T_c/J \sim 0.024$, the temperature at which $\lambda_d \to 1$.

Although we focus here on the use of DMFT to solve the Hubbard Hamiltonian, it is important to note that it has also revolutionized electronic structure calculations (the so-called 'LDA+DMFT' method [64]), since realistic band structures can be incorporated into $\epsilon(\mathbf{p})$ in Eq. 16.

The underlying approximation of DMFT, that the self-energy is independent of momentum, can be systematically improved via extensions such as the Dynamic Cluster Approximation (DCA) [65, 66] and Cluster DMFT [67]. Within the DCA, the self-energy is evaluated on a grid of N_c momentum points. Since they build upon the method as described above, we will not review the details here. However, we do show in Fig. 4 some state-of-the-art results for the d-wave superconducting transition in the 2D Hubbard model [68].

DMFT and its cluster extensions have several very significant advantages over real-space methods like DQMC. Specifically, they have a much better 'sign problem' (although this becomes less true as the cluster size increases) and they work directly in the thermodynamic limit. The latter fact enables them to extract transition temperatures via divergences of appropriate susceptibilities (Fig. 4) without having to make recourse to a laborious finite size scaling analysis as is required in, for example, DQMC [45]. For these reasons, much of our most reliable knowledge of the physics of the Hubbard Hamiltonian in the thermodynamic limit, including the question of the existence of a superconducting state with d-wave symmetry, has been through these approaches.

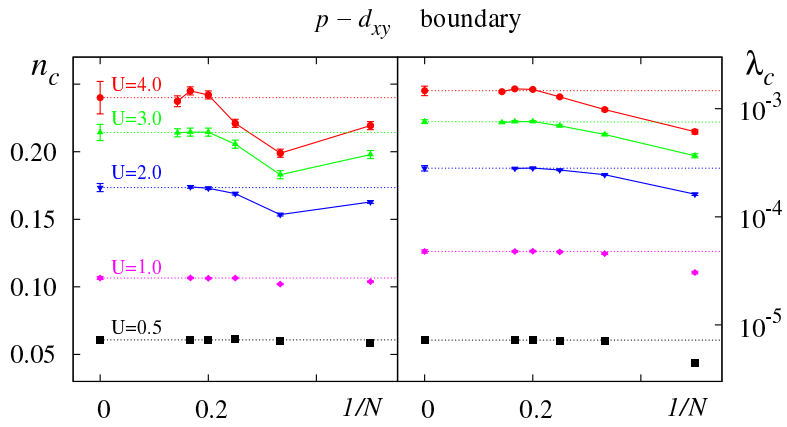

Figure 4: Some diagrammatic QMC results for the square lattice Hubbard model at densities $\langle n \rangle < 0.7$. Critical density (left) and critical coupling constant (right) for the phase boundary between p-wave and d-wave superfluid phases as a function of the expansion order N.

9 Diagrammatic Quantum Monte Carlo

Diagrammatic QMC [21,69–73] begins with a perturbative expansion of the partition function

$$\begin{aligned} Z = \mathrm{Tr}\, e^{-\beta H} &= \mathrm{Tr}\, \mathcal{T} e^{-\beta H_0} \exp\Big[- \int_0^\beta d\tau H_1(\tau) \Big] \\ &= \sum_k (-1)^k \int_0^\beta d\tau_1 \cdots \int_{\tau_{k-1}}^\beta d\tau_k \, \mathrm{Tr}\big[e^{-\beta H_0} H_1(\tau_k) \cdots H_1(\tau_1) \big] \end{aligned} \tag{17}$$

where H_0 and H_1 are the Hubbard model kinetic and potential energy terms respectively. In contrast to DQMC, which samples a Hubbard-Stratonovich or phonon field with a weight given by fermion determinants, diagrammatic QMC instead samples the Feynman diagrams and integration variables (momentum-energy) with which they are constructed. The numbers and positions of the vertices are also sampled through insertion and removal of $\{\tau_l\}$, effectively sampling the variable k in Eq. 17. For a given temperature and interaction strength, there is a peak in the distribution of the order of the diagrams contributing to Eq. 17, which allows for efficient sampling.

As with other numerical methods, significant improvements since its first introduction have been made to diagrammatic QMC, including the analytic summation of all connections to vertices, which reduces the phase space to be explored stochastically and also reduces or even eliminates, in some cases, the sign problem. The replacement of bare interaction vertices by exact two-body scattering amplitudes likewise is a way to perform parts of the diagrammatic sum analytically.

Applications of diagrammatic QMC have been made to the Hubbard model and also to electron-phonon systems [72] and frustrated spin systems [73]. Like DMFT, diagrammatic QMC can be combined with electronic structure theory [74, 75] to provide more accurate modeling of real materials.

10 Transport Properties

Spin and charge transport can be studied using the numerical methods discussed in this report. These properties will have the most relevance to the dopant array experiments at first as measurement capabilities in those measurements are limited.

To study transport properties numerically, we look at the system's response to an external electric or magnetic field that is in general a function of both space and frequency. We calculate the alternating current (AC) in the linear response regime through Kubo's formula, which relates this current to the correlation functions in the unperturbed system [76, 77]. For example, in the absence of any coherent response (Drude weight), the AC conductivity can be written as

$$\sigma_{xx}(\mathbf{q},\omega) = \frac{i}{\omega}\Lambda_{xx}(\mathbf{q},\omega), \tag{18}$$

where ω is the frequency, and $\Lambda_{xx}(\mathbf{q},w)$ is the Fourier transform of the retarded correlation function of the current operator

$$\Lambda_{xx}(\mathbf{q},t-t') = -i\Theta(t-t')\left\langle\left[j_x(-\mathbf{q},t), j_x(\mathbf{q},t')\right]\right\rangle \tag{19}$$

where t and t' are time, Θ is the step function, and $j_x(\mathbf{q},t) = e^{itH}j_x(\mathbf{q})e^{-itH}$ is the time-dependent current operator at wavevector $\mathbf{q}$ (we have taken $\hbar = 1$). The charge current operator can be obtained via the continuity equation and takes the following form for the Hubbard model:

$$j_x(\mathbf{q}) = iJ\sum_{l,\sigma} e^{i\mathbf{q}\cdot\mathbf{r}_l}(c^\dagger_{l+x\sigma}c_{l\sigma} - c^\dagger_{l\sigma}c_{l+x\sigma}), \tag{20}$$

where J is again the hopping amplitude. Taking the uniform limit $\mathbf{q} = 0$, the real part of the AC conductivity, which is a quantity likely measured in the engineered Si experiments, can be simplified to

$$\text{Re }\sigma_{xx}(\omega) = -\frac{2}{\omega}\,\text{Im}\int_0^\infty dt\, e^{i\omega t}\,\text{Im}\,\langle j_x(t)j_x(0)\rangle \tag{21}$$

Other equivalent expressions for Re $\sigma(\omega)$ that use only the real part or both the real and imaginary parts of the current-current correlation function can be derived as well. For example, one can show that [76, 78, 79]

$$\text{Re }\sigma_{xx}(\omega) = \frac{(1-e^{-\beta\omega})}{\omega}\,\text{Re}\int_0^\infty dt\, e^{i\omega t}\,\langle j_x(t)j_x(0)\rangle \tag{22}$$

whose direct current (DC) limit ($\omega \to 0$), takes a simple form of

$$\text{Re }\sigma^{DC}_{xx} = \beta\,\text{Re}\int_0^\infty dt\,\langle j_x(t)j_x(0)\rangle \tag{23}$$

In principle, the time-dependent current correlator can be calculated in the ED or the NLCE in order to obtain the conductivity [79]. However, in the ED for small clusters, the

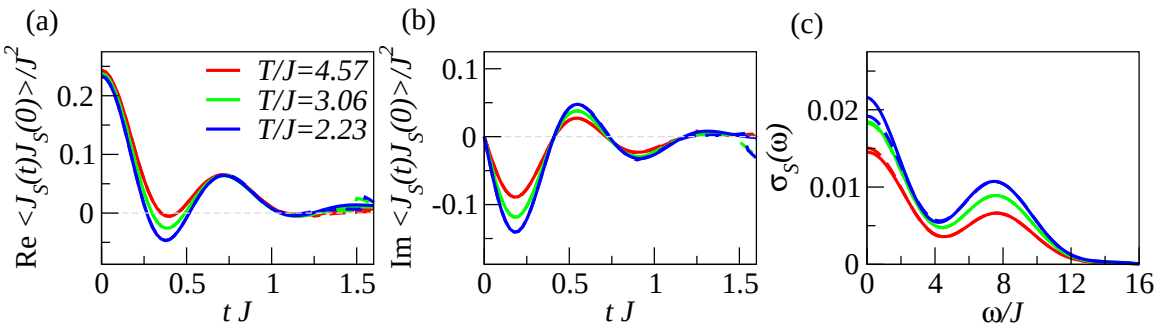

Figure 5: Taken from Ref. [79]. The real time spin current correlation functions and the AC spin conductivity of the Hubbard model are shown for $U/J = 8$ at half filling. The AC spin conductivity is obtained from Eq. 22 (solid lines) and Eq. 21 (dashed lines) at the various temperatures.

correlator is expected to exhibit significant fluctuations at all times due to the boundaries, and therefore, any Fourier transform of the finite-time correlation function can lead to uncertainties in the conductivity. For this reason, it may be advantageous to take the Fourier transform first by explicitly expressing the time dependence of the current correlator [76]. The resulting formula takes the following form, often used in the ED study of the conductivity [80]:

$$\text{Re } \sigma_{xx}(\omega) = \pi \frac{(1 - e^{-\beta\omega})}{\omega Z} \sum_{n,m} e^{-\beta E_n} |\langle n|j_x(0)|m\rangle|^2 \delta(\omega + E_n - E_m), \tag{24}$$

where Z is the partition function, E_n is the eigenenergy of the nth eigenstate of the Hamiltonian, and δ is the delta function. This expression is of course directly analogous to Eq. 22.

In the NLCE, we can work with real time current correlation functions [79]. Even though the convergence of the series at a given temperature can now be lost beyond some maximal time, in the absence of boundary effects for the system in the thermodynamic limit, the fluctuations in time are expected to die off eventually and a Fourier transform of the Green's function in the converged region can still provide a good estimate for the AC conductivity, especially away from the zero frequency limit.

In Fig. 5, we show the AC *spin* conductivity for the Hubbard model in the thermodynamic limit. The spin current is defined similar to the charge current in Eq. (20) and is obtained by including the spin $\sigma/2$ as a multiplying factor inside the sum [79].

Even though the real time dependent quantities are not accessible in equilibrium quantum Monte Carlo methods, such as DQMC, DMFT, DCA, and diagrammatic QMC described earlier, the retarded current Green's function of Eq. (19) can be calculated on the imaginary time axis:

$$\Lambda_{xx}(\mathbf{q}, \tau) = -\langle \mathcal{T} j_{xx}(\mathbf{q}, \tau) j_{xx}(\mathbf{q}, 0) \rangle . \tag{25}$$

The AC conductivity can be obtained by Fourier transforming the imaginary-time Green's function to the Matsubara frequency space and then analytically continuing the imaginary

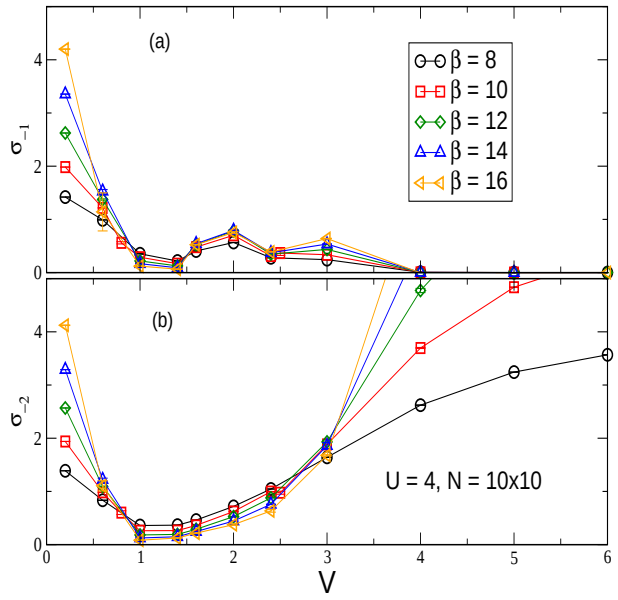

Figure 6: An illustration of DQMC capabilities for obtaining conductivities via analytic continuation. The system being studied is an interface between a Mott insulator and a metal. Simulations were done on 10x10 layers at $U/J = 4$ and five inverse temperatures β.

frequency quantity to the real frequency axis ($i\omega_n \to \omega + \delta$), a process that is numerically ill-defined, but can be accomplished using, e.g., the maximum entropy method. It amounts to taking the inverse of an integral such as an analog of Eq. 6, [81]

$$\Lambda_{xx}(\tau) = \int_{-\infty}^{\infty} \frac{d\omega}{\pi} \frac{-e^{-\tau\omega}}{1 - e^{-\beta\omega}} \text{ Im } \Lambda_{xx}(\omega) \tag{26}$$

An approximate form for the DC conductivity can be worked out for temperatures much lower than a characteristic frequency scale in the system below which the AC conductivity is essentially constant. Starting from Eq. (26), it can be shown that in this regime

$$\sigma_{xx}^{DC} \approx \frac{\beta^2}{\pi} \Lambda_{xx}(\beta/2), \tag{27}$$

a form that can be used as a proxy for the actual DC conductivity of the system. Similar expressions have been used for the electronic spectral function, spin susceptibility, as well as conductivity [81–83]

Another arguably more robust proxy can be derived for the same temperature regime by incorporating information from the curvature of the current Green's function [84, 85].

$$\sigma_{xx}^{DC} \approx \frac{2\pi \Lambda_{xx}(\beta/2)^2}{\Lambda''_{xx}(\beta/2)} \tag{28}$$

Figure 6 shows some DQMC results for the transport in a system with several weakly interacting (metallic) layers, connected to a Mott insulator via an interfacial hopping V. σ_{-1} is the conductivity (obtained via Eq. 27) in the metallic layer most proximate to the insulator. σ_{-2} is the conductivity in the next deepest metallic layer. For V larger than four times the intralayer hopping J, the conductivity σ_{-1} right at the boundary vanishes as a consequence of the formation of magnetic singlets across the boundary. The conductivity deeper within the metal (σ_{-2}) then recovers.

11 Conclusions

Here we have very briefly reviewed some of the technical details of the powerful set of computational approaches developed to solve the Hubbard Hamiltonian over the last three decades. These methods have given tremendous insight into the physics of the model. Unfortunately, one lesson has been that the Hubbard Hamiltonian supports a diverse set of possible low temperature phases, and that these often have free energies which differ by rather small amounts. As a consequence, there is the ongoing concern that seemingly innocuous approximations or finite size effects might affect the conclusions. This observation has driven more and more accurate algorithms, and also attempts such as optical lattice emulation and, potentially, the engineered materials approach of this report. The objective is a careful comparison of theory and experiment which will conclusively determine the strong correlation physics of the Hubbard model.

Of the methods described there, exact diagonalization, Lanczos, the Numerical Linked Cluster Expansion, and Determinant Quantum Monte Carlo all work directly in real space, and have the capability of modeling uncertainties in atomic placement and on-site interaction strength. In addition, they have complementary capabilities in terms of lattice sizes, accessible energy and temperature scales, and ability to draw out transport properties. They therefore are likely to partner well with the first generation of engineered materials experiments. Once the initial testing and comparisons are done, one would expect the full panoply of techniques to be crucial.

References

[1] "Monte Carlo calculations of coupled boson-fermion systems. I," R. Blankenbecler, D.J. Scalapino, and R.L. Sugar, Phys. Rev. D24, 2278 (1981).

[2] "A Novel Technique for the Simulation of Interacting Fermion Systems," S. Sorella, S. Baroni, R. Car, and M. Parinello, Europhys. Lett. 8, 663 (1989).

[3] "'Worm' algorithm in quantum Monte Carlo simulations," N. Prokofév, B. Svistunov, and I. Tupitsyn, Phys. Lett. A238, 253 (1998).

[4] "Cluster algorithm for vertex models," H.G. Evertz, G. Lana, and M. Marcu, Phys. Rev. Lett. 70, 875 (1993).

[5] "The Loop Algorithm," H. G. Evertz, Advances in Physics 52, 1 (2003).

[6] "Quantum Monte Carlo with directed loops," O.F. Syljuasen and A.W. Sandvik, Phys. Rev. E66, 046701 (2002).

[7] "Generalized directed loop method for quantum Monte Carlo simulations," F. Alet, S. Wessel, and M. Troyer, Phys. Rev. E71, 036706 (2005).

[8] "Stochastic Green function algorithm," V.G. Rousseau, Phys. Rev. E77, 056705 (2008).

[9] "Quantum Monte Carlo simulation in the canonical ensemble at finite temperature," K. Van Houcke, S.M.A. Rombouts, and L. Pollet, Phys. Rev. E73, 056703 (2006).

[10] "Loop Updates for Quantum Monte Carlo Simulations in the Canonical Ensemble," S.M.A. Rombouts, K. Van Houcke, and L. Pollet, Phys. Rev. Lett. 96, 180603 (2006).

[11] "Loop algorithms for quantum simulations of fermion models on lattices," N. Kawashima, J.E. Gubernatis, and H.G. Evertz, Phys. Rev. B50, 136 (1994).

[12] "Simulations of Discrete Quantum Systems in Continuous Euclidean Time," B.B. Beard and U.J. Wiese, Phys. Rev. Lett. 77, 5130 (1996).

[13] "Exact quantum Monte Carlo process for the statistics of discrete systems," N.V. Prokofév, B.V. Svistunov, and I.S. Tupitsyn, J. Expt. and Theor. Phys. 64, 911 (1996).

[14] "Exact, complete, and universal continuous-time worldline Monte Carlo approach to the statistics of discrete quantum systems," N.V. Prokofev, B.V. Svistunov, and I.S. Tupitsyn, J. Expt. and Theor. Phys. 87, 310 (1998).

[15] "Application of a continuous time cluster algorithm to the two-dimensional random quantum Ising ferromagnet," H. Rieger and N. Kawashima, Eur. Phys. J. B9, 233 (1999).

[16] "A Quantum Monte Carlo algorithm for non-local corrections to the Dynamical Mean-Field Approximation," M. Jarrell, T. Maier, C. Huscroft, and S. Moukouri, Phys. Rev. B64, 195130 (2001).

[17] "Quantum Monte Carlo simulations and maximum entropy: Dynamics from imaginary time data," J.E. Gubernatis, M. Jarrell, R.N. Silver, and D.S. Sivia, Phys. Rev. B44, 6011 (1991).

[18] "Bayesian Inference and the Analytic Continuation of Imaginary-Time Quantum Monte Carlo Data," M. Jarrell and J.E. Gubernatis, Phys. Rep. 269, 133 (1996).

[19] "Stochastic series expansion method with operator-loop update," A.W. Sandvik, Phys. Rev. B59, R14157 (1999).

[20] "Constrained path Monte Carlo method for fermion ground states," S. Zhang, J. Carlson, and J.E. Gubernatis, Phys. Rev. B55, 7464 (1997).

[21] "Diagrammatic Monte Carlo for correlated fermions," E. Kozik, K. Van Houcke, E. Gull, L. Pollet, N. Prokofév, B. Svistunov and M. Troyer, Europhys. Lett. 90, 10004 (2010).

[22] "Fast update algorithm for the quantum Monte Carlo simulation of the Hubbard model," P.K.V.V. Nukala, T.A. Maier, M.S. Summers, G. Alvarez, and T.C. Schulthess, Phys. Rev. B80, 195111 (2009).

[23] "Submatrix updates for the continuous-time auxiliary-field algorithm," E. Gull, P. Staar, S. Fuchs, P.K.V.V. Nukala, M.S. Summers, T. Pruschke, T.C. Schulthess, and T.A. Maier, Phys. Rev. B83, 075112 (2011).

[24] "Néel temperature and thermodynamics of the half-filled three-dimensional Hubbard model by diagrammatic determinant Monte Carlo," E. Kozik, E. Burovski, V.W. Scarola, and M. Troyer, Phys. Rev. B87, 205102 (2013).

[25] "The Hubbard Model- Recent Results", M. Rasetti, World Scientific, 1991.

[26] "The Hubbard Model," Arianna Montorsi (ed), World Scientific, 1992.

[27] "The Mott Metal-Insulator Transition, Models and Methods", F. Gebhard, Springer 1997.

[28] "Lecture Notes on Electron Correlation and Magnetism", P. Fazekas, World Scientific (1999).

[29] "Competition Between Antiferromagnetic Order and Spin Liquid Behavior in the Two–Dimensional Periodic Anderson Model at Half–Filling," M. Vekic, J.W. Cannon, D.J. Scalapino, R.T. Scalettar, and R.L. Sugar, Phys. Rev. Lett. 74, 2367 (1995).

[30] "Numerical linked-cluster approach to quantum lattice models," M. Rigol, T. Bryant, and R. R. P. Singh, Phys. Rev. Lett. 97, 187202 (2006).

[31] "Numerical linked-cluster algorithms. i. spin systems on square, triangular, and kagomé lattices," M. Rigol, T. Bryant, and R. R. P. Singh, Phys. Rev. E75, 061118 (2007).

[32] "Numerical linked-cluster algorithms. ii. $t-j$ models on the square lattice," M. Rigol, T. Bryant, and R. R. P. Singh, Phys. Rev. E75, 061119, (2007).

[33] "Finite-temperature properties of strongly correlated fermions in the honeycomb lattice," B. Tang, T. Paiva, E. Khatami, and Rigol, Phys. Rev. B88, 125127 (2013).

[34] "Thermodynamics of strongly interacting fermions in two-dimensional optical lattices," E. Khatami and M. Rigol, Phys. Rev. A84, 053611 (2011).

[35] "Effect of particle statistics in strongly correlated two-dimensional hubbard models," E. Khatami and M. Rigol, Phys. Rev. A86, 023633, (2012).

[36] "Short-range correlations and cooling of ultracold fermions in the honeycomb lattice," B. Tang, T. Paiva, E. Khatami, and M. Rigol, Phys. Rev. Lett. 109, 205301 (2012).

[37] "Discrete Hubbard-Stratonovich transformation for fermion lattice models", J.E. Hirsch, Phys. Rev. B28, 4059 (1983).

[38] "Ergodicity at large couplings with the determinant Monte Carlo algorithm", R.T. Scalettar, R.M. Noack, and R.R.P. Singh, Phys. Rev. B44, 10502 (1991).

[39] "On the product of semi-groups of operators," H.F. Trotter, Proc. Amer. Math. Soc. 10, 545 (1959).

[40] "Generalized Trotter's formula and systematic approximants of exponential operators and inner derivations with applications to many-body problems", M. Suzuki, Comm. Math. Phys. 51, 183 (1976).

[41] "New results on Trotter-like approximations", R.M. Fye, Phys. Rev. B33, 6271 (1986).

[42] "Continuous time quantum Monte Carlo method for fermions: beyond auxiliary field framework," A.N. Rubtsov and A.I. Lichtenstein, Pis'ma JETP 80, 67 (2004).

[43] "Continuous-time quantum Monte Carlo method for fermions," A.N. Rubtsov, V.V. Savkin, and A.I. Lichtenstein, Phys. Rev. B72, 035122 (2005).

[44] "Thermodynamics of the 3D Hubbard Model on Approaching the Neel Transition," S. Fuchs, E. Gull, L. Pollet, E. Burovski, E. Kozik, T. Pruschke, and M. Troyer, Phys. Rev. Lett. 106, 030401 (2011).

[45] "Quantum Monte Carlo Study of the 2D Fermion Hubbard Model at Half-Filling," C.N. Varney, C.R. Lee, Z.J. Bai, S. Chiesa, M. Jarrell, and R. T. Scalettar, Phys. Rev. B80, 075116 (2009).

[46] "The Sign Problem in the Numerical Simulation of Many Electron Systems," E.Y. Loh, J.E. Gubernatis, R.T. Scalettar, S.R. White, D.J. Scalapino, and R.L. Sugar, Phys. Rev. B41, 9301 (1990).

[47] "Representation Basis in Quantum Monte Carlo Calculations and the Negative-Sign Problem," N. Hatano and M. Suzuki, Phys. Lett. A163, 246 (1992).

[48] "Vanishing of the negative-sign problem of quantum Monte Carlo simulations in one-dimensional frustrated spin systems," T. Nakamura, Phys. Rev. B57, R3197 (1998).

[49] "Meron-Cluster Solution of Fermion Sign Problems," S. Chandrasekharan and U.-J. Wiese, Phys. Rev. Lett. 83, 3116 (1999).

[50] "Computational complexity and fundamental limitations to fermionic quantum Monte Carlo simulations", M. Troyer and U.-J. Wiese, Phys. Rev. Lett. 94, 170201 (2005).

[51] "Imaginary polarization as a way to surmount the sign problem in ab initio calculations of spin-imbalanced Fermi gases," J. Braun, J-W. Chen, J. Deng, J.E. Drut, B. Friman, C-T. Ma, and Y-D. Tsai, Phys. Rev. Lett. 110, 130404 (2013).

[52] "Geometry dependence of the sign problem in quantum Monte Carlo simulations," V. I. Iglovikov, E. Khatami, and R. T. Scalettar, Phys. Rev. B 92, 045110 (2015).

[53] "Charged magnetic domain lines and the magnetism of high-Tc oxides," J. Zaanen and O. Gunnarsson, Phys. Rev. B40, 7391 (1989).

[54] "Hubbard model in infinite dimensions: A quantum Monte Carlo study", M. Jarrell, Phys. Rev. Lett. 69, 168 (1992).

[55] "The Hubbard Model at Infinite Dimensions: Thermodynamic and Transport Properties," Th. Pruschke, D.L. Cox, and M. Jarrell, Phys. Rev. B47, 3553 (1993).

[56] "Dynamical mean-field theory of strongly correlated fermion systems and the limit of infinite dimensions", A. Georges, G. Kotliar, W. Krauth, and M. Rozenberg, Rev. Mod. Phys 68, 13 (1996).

[57] "Hubbard model in infinite dimensions", A. Georges and G.Kotliar (1992). Phys. Rev. B45, 6479 (1992).

[58] "Correlated Lattice Fermions in $d = \infty$ Dimensions", W. Metzner and D. Vollhardt, Phys. Rev. Lett. 62, 324 (1989)

[59] "Electronic structure calculations with dynamical mean-field theory", G. Kotliar, S.Y. Savrasov, K. Haule; V.S. Oudovenko, O. Parcollet, and C. A. Marianetti, Rev. Mod. Phys. 78, 865 (2006).

[60] "Dynamical mean-field theory for correlated electrons", D. Vollhardt, Ann. Phys. 524, 1 (2012).

[61] "Strongly Correlated Electron Materials: Dynamical Mean-Field Theory and Electronic Structure", A. Georges, AIP Conference Proceedings. American Institute of Physics Conference. Lectures on the Physics of Highly Correlated Electron Systems VIII, 715 3 (2004).

[62] "Electronic Structure Calculations using Dynamical Mean Field Theory", K. Held, Adv. Phys. 56, 829 (2007).

[63] "Dynamical vertex approximation: A step beyond dynamical mean-field theory", A. Toschi, A. Katanin, and K. Held, Phys. Rev. B75, 045118 (2007).

[64] "Realistic investigations of correlated electron systems with LDA+DMFT", K. Held, I.A. Nekrasov, G. Keller, V. Eyert, N. Blümer, A.K. McMahan, R.T. Scalettar, Th. Pruschke, V.I. Anisimov, and D. Vollhardt, Psi-k Newsletter 56, 65 (2003).

[65] "Dynamical cluster approximation: Nonlocal dynamics of correlated electron systems," M. H. Hettler, M. Mukherjee, M. Jarrell, and H. R. Krishnamurthy, Phys. Rev. B61, 12739 (2000).

[66] "Quantum cluster theories", T. Maier, M. Jarrell, T. Pruschke, and M.H. Hettler, Rev. Mod. Phys. 77, 1027 (2005).

[67] "Cluster Dynamical Mean Field Theory of the Mott Transition," H. Park, K. Haule, and G. Kotliar, Phys. Rev. Lett. 101, 186403 (2008).

[68] "Two-particle correlations in a dynamic cluster approximation with continuous momentum dependence: Superconductivity in the two-dimensional Hubbard model," P. Staar, T. Maier, and T.C. Schulthess, Phys. Rev. B89, 195133 (2014).

[69] "Feynman diagrams versus Fermi-gas Feynman emulator," K. Van Houcke, F. Werner, E. Kozik, N. Prokofév, B. Svistunov, M. Ku, A. Sommer, L. Cheuk, A. Schirotzek, and M. Zwierlein, Nature Physics 8, 366 (2012).

[70] "Emergent BCS regime of the two-dimensional fermionic Hubbard model: ground-state phase diagram," Y. Deng, E. Kozik, N. V. Prokofév, and B. V. Svistunov, Europhys. Lett. 110, 57001 (2015).

[71] "p-wave Superfluidity by Spin-Nematic Fermi Surface Deformation," J Gukelberger, E. Kozik, L. Pollet, N. Prokofév, M. Sigrist, B. Svistunov, and M. Troyer, Phys. Rev. Lett. 113, 195301 (2014).

[72] "Diagrammatic Monte Carlo method for many-polaron problems," A. S. Mishchenko, N. Nagaosa, and N. Prokofév, Phys. Rev. Lett. 113, 166402 (2014).

[73] "Bold Diagrammatic Monte Carlo Method Applied to Fermionized Frustrated Spins", S. A. Kulagin, N. Prokofév, O. A. Starykh, B. Svistunov, and C. N. Varney, Phys. Rev. Lett. 110, 070601 (2013).

[74] "Many-body perturbation theory approach to the electron-phonon interaction with density-functional theory as a starting point," Andrea Marini, S. Poncé, and X. Gonze Phys. Rev. B91, 224310 (2015).

[75] "Diagrammatic Monte Carlo and GW Approximation for Jellium and Hydrogen Chain," K. Van Houcke, I.S Tupitsyn, and N.V. Prokofév, *Handbook of Materials Modeling: Methods: Theory and Modeling*, 1 (2018).

[76] G. D. Mahan, *Many-Particle Physics*. Plenum Press, 1981.

[77] "Insulator, metal, or superconductor: The criteria," D. J. Scalapino, S. R. White, and S. Zhang, Phys. Rev. B47, 7995 (1993).

[78] "Transport properties of the one-dimensional hubbard model at finite temperature," C. Karrasch, D. M. Kennes, and J. E. Moore, Phys. Rev. B90, 155104 (2014).

[79] "Spin transport in a mott insulator of ultracold fermions," M. A. Nichols, L. W. Cheuk, M. Okan, T. R. Hartke, E. Mendez, T. Senthil, E. Khatami, H. Zhang, and M. W. Zwierlein, (2018).

[80] "Optical conductivity of the hubbard model at finite temperature," J. A. Riera and E. Dagotto, Phys. Rev. B50, 452 (1994).

[81] "Deviations from fermi-liquid behavior above T_c in 2d short coherence length superconductors," N. Trivedi and M. Randeria, Phys. Rev. Lett. 75, 312 (1995).

[82] "Pairing and spin gap in the normal state of short coherence length superconductors," M. Randeria, N. Trivedi, A. Moreo, and R. T. Scalettar, Phys. Rev. Lett. 69, 2001 (1992).

[83] "Superconductor-insulator transition in a disordered electronic system," Phys. Rev. B54, N. Trivedi, R. T. Scalettar, and M. Randeria, 3756 (1996).

[84] "Strange metallicity in the doped Hubbard model," E. W. Huang, R. Sheppard, B. Moritz, and T. P. Devereaux, (2018).

[85] "Superconductivity and non-fermi liquid behavior near a nematic quantum critical point," S. Lederer, Y. Schattner, E. Berg, and S. A. Kivelson, Proc. Natl. Acad. Sci. (U.S.A.) 114, 4905 (2017).

[86] "Monte Carlo Study of Entropy for Face-Centered Cubic Ising Antiferromagnets, K. Binder, Z. Phys. 45, 61 (1981).

[87] "Interaction-induced adiabatic cooling for antiferromagnetism in optical lattices," A.M. Dare, L. Raymond, G. Albinet, and A.M.S. Tremblay, Phys. Rev. B76, 064402 (2007).